

Emerging symmetric strain response and weakening nematic fluctuations in strongly hole-doped iron-based superconductors

P. Wiecki¹, M. Frachet¹, A.-A. Haghighirad¹, T. Wolf¹, C. Meingast¹, R. Heid¹, and A. E. Böhmer^{1,2,*}

¹Karlsruhe Institute of Technology, Institute for Quantum Materials and Technologies, 76021 Karlsruhe, Germany

²Institut für Experimentalphysik IV, Ruhr-Universität Bochum, 44801 Bochum, Germany

*anna.boehmer@kit.edu

ABSTRACT

Electronic nematicity is often found in unconventional superconductors, suggesting its relevance for electronic pairing. In the strongly hole-doped iron-based superconductors, the symmetry channel and strength of the nematic fluctuations, as well as the possible presence of long-range nematic order, remain controversial. Here, we address these questions using transport measurements under elastic strain. By decomposing the strain response into the appropriate symmetry channels, we demonstrate the emergence of a giant in-plane symmetric contribution, associated with the growth of both strong electronic correlations and the sensitivity of these correlations to strain. We find weakened remnants of the nematic fluctuations that are present at optimal doping, but no change in the symmetry channel of nematic fluctuations with hole doping. Furthermore, we find no evidence for a nematic-ordered state in the AFe_2As_2 ($A = \text{K, Rb, Cs}$) superconductors. These results revise the current understanding of nematicity in hole-doped iron-based superconductors.

Introduction

Nematicity, the breaking of rotational symmetry by electronic interactions, has by now been observed in a variety of unconventional superconductors. In addition to iron-based superconductors with almost ubiquitous nematicity^{1,2}, nematicity is discussed in the context of cuprate high- T_c superconductors^{3–12}, heavy-fermion superconductors^{13,14}, intercalated Bi_2Se_3 topological superconductors^{15–18} and even twisted bilayer graphene¹⁹. Furthermore, it has been theoretically suggested that nematic fluctuations may enhance pairing and therefore be an important ingredient for high- T_c superconductivity^{20–23}.

In iron-based superconductors, nematicity has been intensively studied in the vicinity of the parent compound BaFe_2As_2 because the stripe-type antiferromagnetic ground state inherently breaks the C_4 rotational symmetry of the high-temperature tetragonal phase^{1,2,24,25}, corresponding to a nematic degree of freedom. The accompanying structural distortion is in the B_{2g} channel of the tetragonal D_{4h} point group. In electron-doped BaFe_2As_2 , the structural distortion occurs at a higher temperature than the antiferromagnetic state, creating a long-range, nematic-ordered phase. Nematic fluctuations of B_{2g} symmetry are observed near optimal doping in both hole- and electron-doped BaFe_2As_2 ^{26,27}. Such fluctuations have frequently been studied using elastoresistance, the strain dependence of electrical resistivity^{1,28,29}.

The parent compound BaFe_2As_2 nominally has a $3d^6$ Fe configuration. With hole doping the Fe electron configuration begins to approach the half-filled $3d^5$, where a Mott insulating state is expected theoretically^{30–32}. Indeed, signatures of strong electronic correlations and orbital-selective Mott behavior have been observed in the isoelectronic $3d^{5.5}$ series AFe_2As_2 ($A = \text{K, Rb, Cs}$), including an enhanced Sommerfeld coefficient and signs of a coherence-incoherence crossover^{33–35}. On the basis of the strong increase of electronic correlations with increasing alkali ion size in AFe_2As_2 ($A = \text{K, Rb, Cs}$), it has further been proposed that these compounds lie near a QCP associated with the suppression of a (thus far unobserved) ordered phase, possibly related to the $3d^5$ Mott insulator^{36,37}. Furthermore, the electronic correlations in AFe_2As_2 have been found to be highly sensitive to in-plane strain^{34,36}.

The fate of nematicity in the strongly hole-doped iron-based superconductors remains controversial. In the $\text{Ba}_{1-x}\text{K}_x\text{Fe}_2\text{As}_2$ series, the elastic softening associated with the B_{2g} nematic fluctuations decreases with hole doping and is no longer observed for $x \geq 0.82$ ²⁷. Several recent studies have suggested a change to nematic fluctuations of B_{1g} symmetry in the $3d^{5.5}$ compounds, in contrast to the pervasive B_{2g} nematic fluctuations observed at optimal doping^{38–44}. Furthermore, an ordered B_{1g} nematic phase has been proposed in RbFe_2As_2 based on a maximum in the elastoresistance³⁹ and an asymmetry observed in low-temperature STM⁴⁰. However, the study of nematic fluctuations in these compounds by elastoresistance is complicated by the emergence

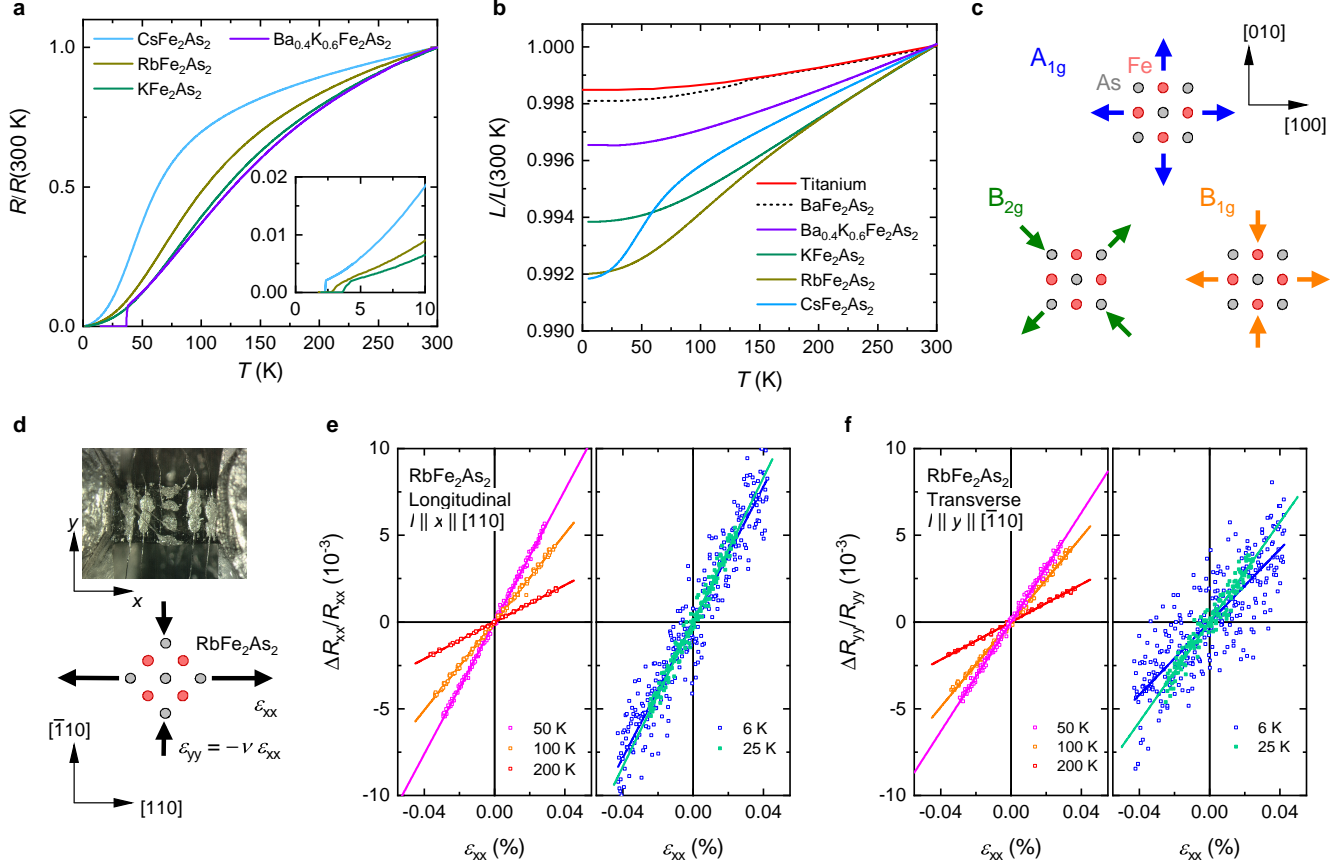


Figure 1. Basic material properties and experimental setup. **a** Normalized electrical resistance as a function of temperature. Inset: zoom of superconducting transitions. **b** In-plane sample length changes as a function of temperature³⁴. Titanium and BaFe₂As₂⁴⁸ are shown for comparison. **c** Sketch of the deformations in the Fe plane corresponding to the indicated irreducible representations. **d** Photograph of a RbFe₂As₂ sample mounted between titanium plates in the strain cell. The uniaxial stress axis is defined to be *x*. In this example, strain is applied along [110] and the sample experiences *A*_{1g} + *B*_{2g} strain. *v* is the in-plane Poisson ratio of the sample. **e-f** Longitudinal and transverse elasto-resistance curves at indicated temperatures. Lines are linear fits.

of the strong electronic correlations, which create a significant contribution in the in-plane symmetric *A*_{1g} channel⁴⁵. In such a case, it is essential to properly decompose the contributions in different symmetry channels by comparing the resistance changes both longitudinal and transverse to the stress axis^{45–47}. In addition, the extreme thermal expansion of these samples (Fig. 1b) poses an experimental challenge for controlled measurements under elastic strain⁴⁵.

In this work, we present comprehensive elasto-resistance measurements on the hole-doped iron-based superconductors Ba_{0.4}K_{0.6}Fe₂As₂ and AFe₂As₂ (A = K, Rb, Cs) carried out in a piezoelectric-based strain cell capable of full control over the strain state of the sample. We find a monotonic increase of the *A*_{1g} response with hole doping and increasing alkali ion size. In contrast, the *B*_{2g} elasto-resistance, a measure of the *B*_{2g} nematic susceptibility, weakens with hole-doping. The *B*_{1g} elasto-resistance shows no sign of a divergence, thus there is no indication of the emergence of a *B*_{1g}-type nematic instability with increasing hole doping. Furthermore, we find a clear correspondence between the low-temperature elasto-resistance and the electronic Grüneisen parameter if the elasto-resistance coefficient is defined based only on the temperature dependent part of the resistance.

Results

Elastoresistance measurements

The freestanding electrical resistance of our samples is displayed in Fig. 1a. For elasto-resistance measurements, the sample is mounted in a strain cell composed of titanium (Fig. 1d). Fig. 1b displays the length of the samples as a function of temperature, along with titanium for comparison. We see that the hole-doped samples shrink much more than the titanium apparatus on

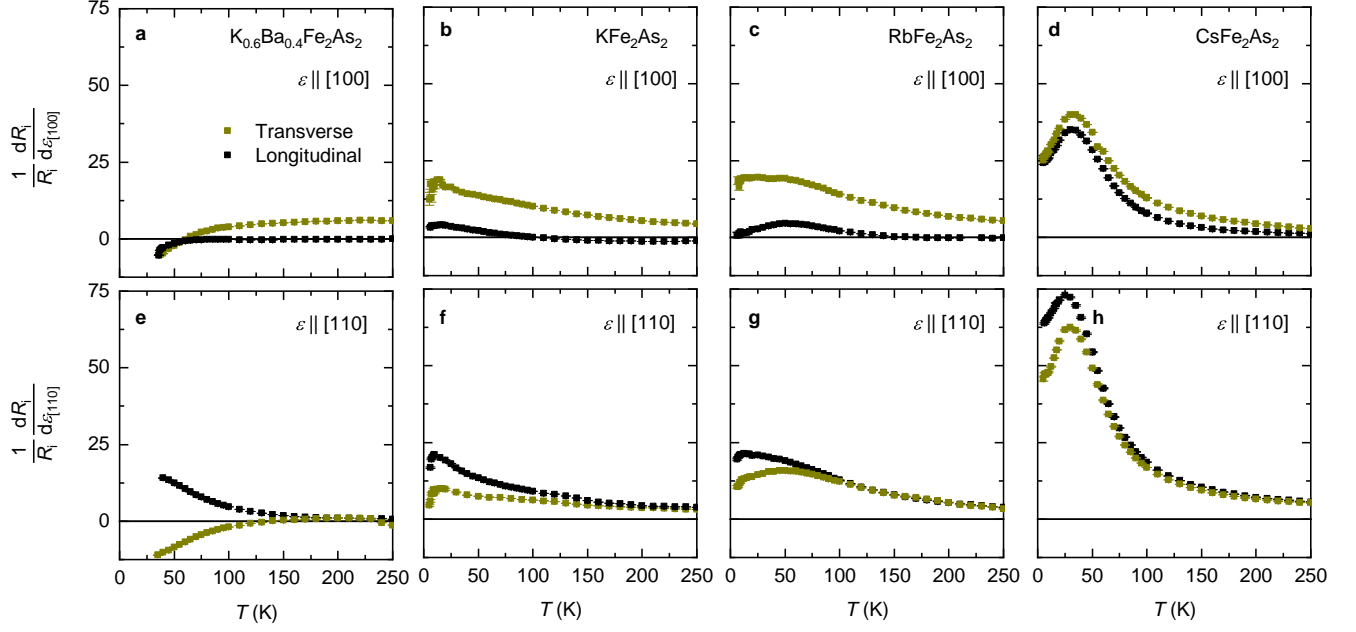


Figure 2. Elastoresistance of strongly hole-doped iron based superconductors. Longitudinal and transverse elastoresistance with the strain direction $\epsilon_{xx}||[100]$ (a-d) and $\epsilon_{xx}||[110]$ (e-h) for indicated samples arranged by column. Error bars indicate one standard deviation.

cooling. Thus, the samples can be maintained near neutral strain on cooling by adjusting the distance between the sample mounting plates in the strain cell based on the thermal expansion difference between the sample and titanium (see Methods). We place eight electrical contacts on the sample so that both longitudinal and transverse elastoresistance can be measured in the same experimental run (Fig. 1d). Raw elastoresistance data on RbFe_2As_2 obtained in this way are shown in Figs. 1e,f as an example.

In Figs. 2 a-h we present the longitudinal and transverse elastoresistance for all samples. Here, the elastoresistance is defined, for the moment, simply as $m_{ii,xx} = (1/R_{ii})dR_{ii}/d\epsilon_{xx}$, where $i = x$ corresponds to the longitudinal and $i = y$ corresponds to the transverse elastoresistance. The strain is applied along $x||[100]$ (Figs. 2 a-d) or $x||[110]$ (Figs. 2 e-h). When strain is applied along $[100]$ the transverse elastoresistance is larger than the longitudinal over most of the temperature range for all samples. In contrast, for strain applied along $[110]$ we observe that the longitudinal and transverse elastoresistance are equal at high temperature, while the longitudinal becomes larger at low temperature, for all samples. In the case of $\text{Ba}_{0.4}\text{K}_{0.6}\text{Fe}_2\text{As}_2$ with strain along $[110]$ (Fig. 2 e), the longitudinal and transverse elastoresistance have opposite sign. This is the expected behavior for dominant B_{2g} nematic fluctuations⁴⁶. In contrast, in the $3d^{5.5}$ superconductors AFe_2As_2 ($\text{A}=\text{K}, \text{Rb}, \text{Cs}$) both the longitudinal and transverse elastoresistance are positive at all temperatures.

We note significant drops in the elastoresistance on decreasing temperature below ~ 15 K for both transverse and longitudinal, most notably in KFe_2As_2 and RbFe_2As_2 (Figs. 2 b,c,f,g). These anomalies are rather broad (as also visible in Fig. 4c with an enhanced scale) and we do not associate them with a phase transition, since no hint of a phase transition is seen in either $R(T)$ or the thermal expansion $L(T)$ (Fig. 1), nor indeed in the respective temperature derivatives $dR(T)/dT$ and $dL(T)/dT$ (Supplemental Figure). Rather, as explained below in relation to Fig. 4, the drop in elastoresistance results from the sample's resistance becoming comparable to its residual resistance. Note, however, that the broad peak in CsFe_2As_2 at ~ 35 K is a pronounced manifestation of the coherence-incoherence crossover in this material.

Physical mechanism for strain dependence of resistance

To obtain a better physical understanding of the elastoresistance, it is useful to take a complementary view and study the resistance as a function of temperature at fixed strain. This is shown in Fig. 3a, taking KFe_2As_2 as an example. At low temperatures, the data can be fit to the standard Fermi liquid form $R = R_0 + AT^2$. The coefficient A is a measure of electronic correlations and effective mass, as given by the Kadowaki-Woods relation for a Fermi liquid $A \propto \gamma^2$, where γ is the Sommerfeld coefficient. The fit parameters R_0 and A are shown as a function of strain in Figs. 3b,c. We observe that the coefficient A increases linearly with strain, while the residual resistance R_0 is strain independent within experimental uncertainty. We have similarly confirmed that R_0 is also strain independent in CsFe_2As_2 .

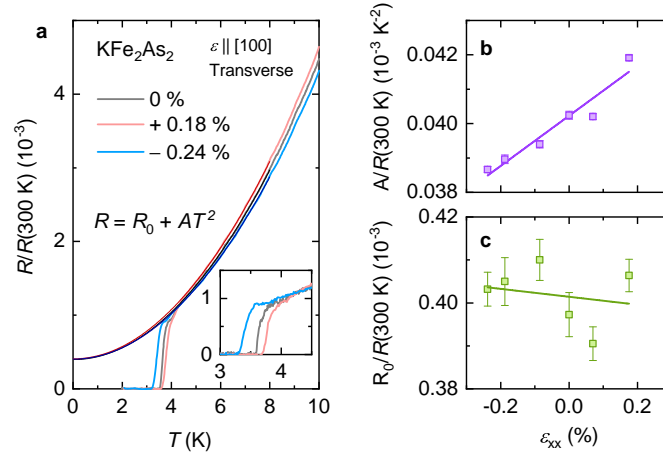


Figure 3. Resistance at fixed strain. **a**, Normalized resistance of KFe_2As_2 as a function of temperature at fixed strains, along with fits to the indicated fitting function. Inset: zoom of superconducting transitions. **b**, Strain dependence of the fit parameter A , measuring electronic correlations and effective mass. **c**, Strain dependence of the fit parameter R_0 , the residual resistance. Lines in **b**, **c** are linear fits.

From the Kadowaki-Woods relation, the increase of A with strain is consistent with the large positive $d\gamma/d\varepsilon$ inferred from thermal expansion measurements^{34,36} (see Methods) and LDA+DMFT calculations⁴⁹. The increase of A under tensile strain ($\varepsilon > 0$) is also consistent with the increase of the Sommerfeld coefficient in unstrained AFe_2As_2 ($A = \text{K, Rb, Cs}$) (Fig. 1a) from $A = \text{K}$ to $A = \text{Cs}$. Namely, the increasing alkali ion size from K to Cs creates a negative chemical pressure, reducing bandwidths and enhancing correlations. Consistently, hydrostatic pressure reduces A in KFe_2As_2 ⁵⁰. Furthermore, we observe that T_c increases with tensile strain. The strain dependence of T_c is in rough quantitative agreement with inferences based on thermodynamic measurements³⁶ (see Methods).

In RbFe_2As_2 and CsFe_2As_2 , we find that the resistance at low temperature can be fit to $R = R_0 + AT^n$, but with an exponent $n < 2$ (Fig. 4a). This is consistent with the non-Fermi liquid behavior seen at low temperature in these samples by NMR³⁷. In Fig. 4b, we show the derivative $dR/d\varepsilon$ as a function of temperature for the case of RbFe_2As_2 with strain $\parallel[110]$ as a representative example. Taking R_0 to be independent of strain, $dR/d\varepsilon = (dA/d\varepsilon)T^n$. Consistently, we find that $dR/d\varepsilon$ can be fit to $B + CT^n$ with the same exponent n as the resistance and an intercept B consistent with zero. In this situation, if the elastoresistance is simply defined as $m = (1/R)dR/d\varepsilon$ as is commonly done (see Fig. 2), we obtain $m = (dA/d\varepsilon)T^n/(R_0 + AT^n)$. Clearly, $m \rightarrow 0$ as $T \rightarrow 0$, as shown in Fig. 4c. As a consequence, the elastoresistance starts to drop on cooling when the residual resistance becomes a significant fraction of the total resistance below 15 K, as noted earlier (Fig. 2). If instead the elastoresistance is redefined based on only the temperature dependent contribution to the resistance as $\bar{m} = [1/(R - R_0)]dR/d\varepsilon$, we obtain $\bar{m} \rightarrow (dA/d\varepsilon)/A$ at low temperature (Fig. 4c). Note that these arguments are valid for any n . A similar approach has been applied in the analysis of elastoresistance data in YbRu_2Ge_2 ⁵¹.

The redefined elastoresistance \bar{m} produces more physically meaningful results at low temperature. For example, in the special case of $n = 2$ where $A \propto \gamma^2$, $\bar{m}(T \rightarrow 0)$ is given by $(dA/d\varepsilon)/A = (d\gamma^2/d\varepsilon)/\gamma^2 = 2(d\gamma/d\varepsilon)/\gamma$, which is proportional to the Grüneisen parameter $\Gamma \equiv (d\gamma/d\varepsilon)/\gamma$ for the Sommerfeld coefficient γ . Γ is a measure of the strain dependence of an energy scale. Its divergence is a central characteristic of a strain-tuned quantum critical point^{48,52,53}, as previously discussed in these materials³⁶.

Having understood the longitudinal and transverse elastoresistance data, we now calculate the symmetry-decomposed elastoresistance coefficients \bar{m}_α , where α represents the irreducible representation of the tetragonal D_{4h} point group. These coefficients determine the resistance changes associated with the pure symmetric strains illustrated schematically in Fig. 1c. In terms of the experimental data, $\bar{m}_{A_{1g}}$ is proportional to the sum of the longitudinal and transverse elastoresistance, while $\bar{m}_{B_{1g}}$ ($\bar{m}_{B_{2g}}$) is proportional to the difference when $\varepsilon \parallel[100]$ ($\varepsilon \parallel[110]$) (see Methods). The resulting symmetry-decomposed elastoresistance coefficients are shown in Fig. 5. The in-plane symmetric coefficient $\bar{m}_{A_{1g}}$ (Fig. 5a) strongly increases in magnitude with hole doping from $\text{Ba}_{0.4}\text{K}_{0.6}\text{Fe}_2\text{As}_2$ to KFe_2As_2 and further with tensile chemical pressure from KFe_2As_2 to CsFe_2As_2 . Furthermore, $\bar{m}_{A_{1g}}$ of CsFe_2As_2 has a strong temperature dependence, with an increase on cooling and a broad peak near 30 K. This temperature dependence is reminiscent of the coherence-incoherence crossover observed in the thermal expansion coefficient of this material^{34,45}. The coefficients $\bar{m}_{B_{2g}}$ (Fig. 5b) and $\bar{m}_{B_{1g}}$ (Fig. 5c) are significantly smaller in magnitude than $\bar{m}_{A_{1g}}$, except for the case of $\bar{m}_{B_{2g}}$ in $\text{Ba}_{0.4}\text{K}_{0.6}\text{Fe}_2\text{As}_2$. For all samples, $\bar{m}_{B_{2g}}$ is near zero at high temperature and displays a divergent increase on cooling. The positive sign of $\bar{m}_{B_{2g}}$ is opposite to that of BaFe_2As_2 , consistent with

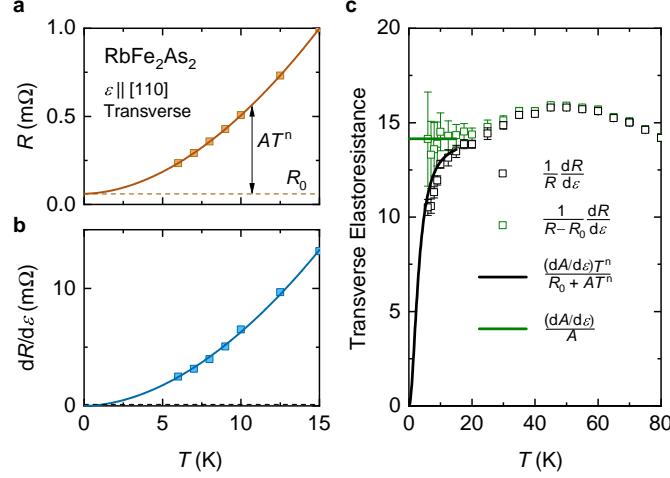


Figure 4. Redefinition of of elastoresistance based on the temperature-dependent resistance contribution **a**, The resistance of a particular RbFe_2As_2 crystal at temperatures where elastoresistance was measured. The solid line is a fit of these points to $R = R_0 + AT^n$ (here $n = 1.84$). The dashed line represents the residual resistance R_0 . **b**, The strain derivative of the sample resistance at selected temperatures. The solid line is a fit of these points to $dR/d\varepsilon = B + CT^n$ (again $n = 1.84$). B is consistent with zero within uncertainty. The dashed line gives an upper limit on B , from the fit uncertainty. **c**, Elastoresistance calculated as $m = (1/R)dR/d\varepsilon$ (black) and $\bar{m} = [1/(R - R_0)]dR/d\varepsilon$ (green). The error bars on $[1/(R - R_0)]dR/d\varepsilon$ reflect the uncertainty in the estimation of R_0 . The solid lines show the same quantities instead calculated from the fitted functions in **a,b**.

observed sign-change of resistivity anisotropy upon K substitution in $\text{Ba}_{1-x}\text{K}_x\text{Fe}_2\text{As}_2$ ⁵⁴. We also note that both $\bar{m}_{B_{1g}}$ and $\bar{m}_{B_{2g}}$ of $\text{Ba}_{0.6}\text{K}_{0.4}\text{Fe}_2\text{As}_2$ are similar in magnitude and sign to $\text{CaKFe}_4\text{As}_4$, which is isoelectronic to $\text{Ba}_{0.5}\text{K}_{0.5}\text{Fe}_2\text{As}_2$ ^{55,56}. The coefficient $\bar{m}_{B_{1g}}$ is non-zero at high temperature and decreases roughly linearly on cooling in RbFe_2As_2 and KFe_2As_2 . In CsFe_2As_2 and $\text{Ba}_{0.4}\text{K}_{0.6}\text{Fe}_2\text{As}_2$ we observe an upturn at low temperature. The temperature dependence of $\bar{m}_{B_{1g}}$ shows no sign of a divergence in any of our samples.

Discussion

We discuss first the in-plane symmetric coefficient $\bar{m}_{A_{1g}}$ (Fig. 5a). Since the resistance reflects the electronic entropy and correlations in these materials^{35,45}, the increase of $\bar{m}_{A_{1g}}$ from KFe_2As_2 to CsFe_2As_2 indicates that the strain sensitivity of the electronic correlations increases as a result of this chemical substitution. This is consistent with the increase in the strain derivative of the Sommerfeld coefficient $\partial\gamma/\partial\varepsilon$ observed in thermodynamic measurements^{34,36}. Therefore, the origin of the large A_{1g} elastoresistance is the high strain sensitivity of the electron correlations associated with the orbital-selective Mott behavior. As a consequence, the temperature and substitution dependence of the A_{1g} coefficient show a strong similarity to that of the thermal expansion coefficient^{34,45} (Supplementary Information).

We turn now to the coefficients $\bar{m}_{B_{2g}}$ (Fig. 5b) and $\bar{m}_{B_{1g}}$ (Fig. 5c) corresponding to symmetry-breaking strain. They are proportional to the nematic susceptibility in the respective symmetry channels¹, though the proportionality constant may become temperature and material dependent⁵⁵. Note that the underdoped BaFe_2As_2 compounds are characterized by a diverging $\bar{m}_{B_{2g}}$. For all samples, $\bar{m}_{B_{2g}}$ is near zero at high temperature and displays divergent increase on cooling. In AFe_2As_2 ($A = \text{K, Rb, Cs}$), $\bar{m}_{B_{2g}}$ is smaller than in $\text{Ba}_{0.4}\text{K}_{0.6}\text{Fe}_2\text{As}_2$ but has a similar temperature dependence, strongly suggesting that we are observing the remnants of the B_{2g} nematic fluctuations found in lightly-doped BaFe_2As_2 . The temperature dependence of the coefficient $\bar{m}_{B_{1g}}$ does not show a divergence with decreasing temperature, an indication that the AFe_2As_2 ($A = \text{K, Rb, Cs}$) compounds are not near a B_{1g} nematic instability. The evolution of $\bar{m}_{B_{1g}}$ and $\bar{m}_{B_{2g}}$ show no indication of a change from B_{2g} to B_{1g} nematic fluctuations in hole-doped iron based superconductors, in contrast to previous studies^{39–43}. Further, nematic fluctuations of XY, as opposed to Ising, character have been proposed in the $\text{Ba}_{1-x}\text{Rb}_x\text{Fe}_2\text{As}_2$ series in the $0.6 < x < 0.8$ doping range³⁹. Whereas we do find that $\bar{m}_{B_{1g}}$ and $\bar{m}_{B_{2g}}$ have similar magnitude in this doping range (in $\text{Ba}_{0.4}\text{K}_{0.6}\text{Fe}_2\text{As}_2$ in our case), their distinct temperature dependence is inconsistent with XY nematic fluctuations.

A phase transition to a long-range ordered B_{1g} nematic ordered phase below 40 K has been proposed in RbFe_2As_2 based on a maximum in the longitudinal elastoresistance measured along $[100]$ ³⁹. The symmetry decomposition of the elastoresistance reveals that such a maximum occurs in the A_{1g} channel, which we associate with the coherence/incoherence crossover and not a

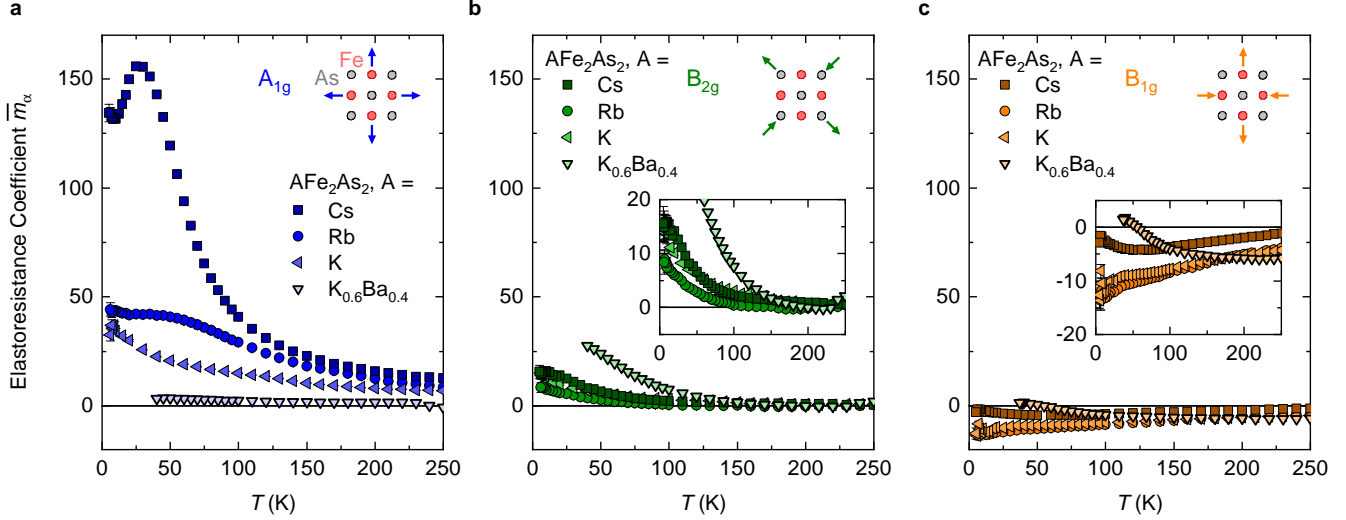


Figure 5. Symmetry-decomposed elastoresistance coefficients. Calculated with the redefined \bar{m}_α (see text). **a**, $\bar{m}_{A_{1g}}$ calculated from $\epsilon_{xx}||[110]$ data. **b**, $\bar{m}_{B_{2g}}$. **c**, $\bar{m}_{B_{1g}}$. The strain symmetry channels are illustrated in the upper right of each panel. The insets in panels **b** and **c** show a zoomed view. The error bars take into account the uncertainty in R_0 . Due to large uncertainties in R_0 for the high- T_c sample $\text{Ba}_{0.4}\text{K}_{0.6}$, we have plotted m_α instead of \bar{m}_α for this sample (points with thick edges).

phase transition. Consistently, the resistance and thermal expansion³⁴ data show no sign of a phase transition in RbFe_2As_2 (Fig. 1a and Supplementary Figure).

Our results are summarized in Fig. 6. In this phase diagram, we plot the values of the elastoresistance coefficients at 40 K as a function of substitution, with both the hole-doped series $\text{Ba}_{1-x}\text{K}_x\text{Fe}_2\text{As}_2$ and the isoelectronic $3d^{5.5}$ series AFe_2As_2 ($A = \text{K}, \text{Rb}, \text{Cs}$) on the same horizontal axis. 40 K is chosen so that the high- T_c sample can be included. The hashed region $0.6 < x < 0.8$ denotes the doping range where a significant change of behavior has been observed, including a Lifshitz transition^{57–60} and proposed broken time-reversal symmetry in the superconducting state^{61–63}, as well as the proposed XY nematic state in the Rb-doped series ($\text{Ba}_{1-x}\text{Rb}_x\text{Fe}_2\text{As}_2$)³⁹. Our results suggest that this doping range coincides with the emergence of an enhanced A_{1g} elastoresistance. Recalling that $\bar{m}_{A_{1g}}$ is expected to reflect the in-plane Grüneisen parameter Γ_a at low temperature, we plot Γ_a alongside $\bar{m}_{A_{1g}}$ (40 K) in Fig. 6. The agreement confirms that the $\bar{m}_{A_{1g}}$ component of elastoresistance is associated with the strong electronic correlations observed in thermodynamic measurements.

We stress that we observe, nevertheless, the remnant of the B_{2g} nematic fluctuations of the optimally-doped regime even in fully substituted samples with $3d^{5.5}$ electronic configuration. We also observe signatures of possible weak nematic fluctuations in the B_{1g} channel, but we do not observe a change from B_{2g} -dominant to B_{1g} -dominant nematic fluctuations with doping and we find no evidence for a bulk nematic state in any of our samples. These results revise the current understanding of nematicity in hole-doped iron based superconductors and raise some new points. First, neither B_{1g} nor B_{2g} nematic fluctuations depend strongly on the alkali ion size in AFe_2As_2 ($A = \text{K}, \text{Rb}, \text{Cs}$). In contrast, the strong correlations related to the orbital-selective Mott behavior seen in the A_{1g} channel increase dramatically with increasing alkali ion size. The contrasting behavior indicates that the orbital-selective Mott physics does not cause the nematic fluctuations. Similarly, the heavy-fermion superconductor URu_2Si_2 has recently been shown to have a large symmetric elastoresistance without nematicity⁶⁴. Secondly, we find that the B_{2g} nematic fluctuations are surprisingly robust, persisting at high hole doping even beyond the Lifshitz transition where the electron pocket of the Fermi surface and the corresponding nesting properties are lost, and magnetic fluctuations become incommensurate. This may be related to why the superconducting dome stretches so far in these compounds.

To conclude, we reflect on the different physical mechanisms responsible for the observed strain-induced resistance changes. In $\text{Ba}_{0.4}\text{K}_{0.6}\text{Fe}_2\text{As}_2$ with a sizeable nematic susceptibility, anisotropic strains change the measured resistance by favoring the resistance of one in-plane direction over the other, as nematic order causes a resistance anisotropy. In CsFe_2As_2 , by contrast, symmetric strains directly modulate the strength of electron correlations and effective mass causing changes in average in-plane resistance.

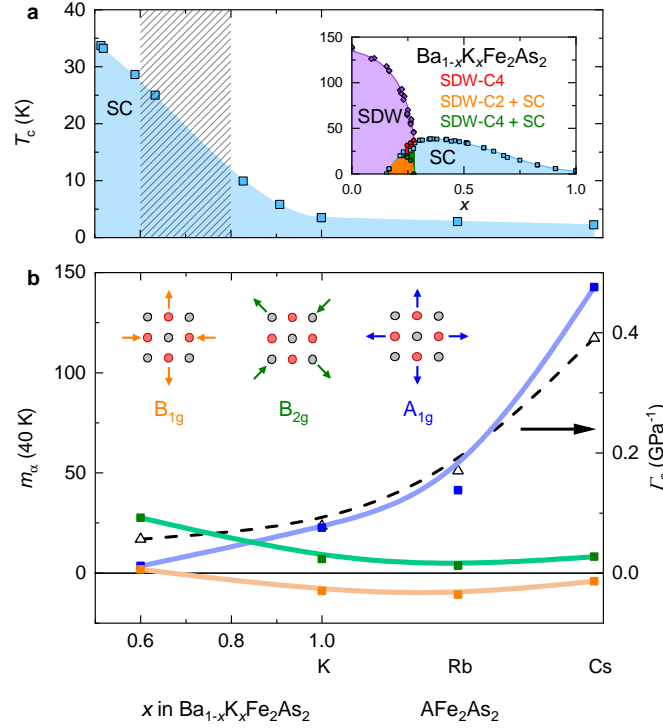


Figure 6. Evolution of the elastoresistance coefficients with chemical substitution. **a** Phase diagram of the hole-doped series $\text{Ba}_{1-x}\text{K}_x\text{Fe}_2\text{As}_2$ for $x > 0.3$ and the isoelectronic series $3d^{5.5}$ series AFe_2As_2 ($\text{A} = \text{K}, \text{Rb}, \text{Cs}$) on the same horizontal axis. The hashed area denotes the doping range of a Lifshitz transition^{57–60} and proposed broken time-reversal symmetry in the SC state^{61–63}. XY-type nematic fluctuations were suggested in the same doping range in the related system $\text{Ba}_{1-x}\text{Rb}_x\text{Fe}_2\text{As}_2$ ³⁹. Inset: full thermodynamic phase diagram of $\text{Ba}_{1-x}\text{K}_x\text{Fe}_2\text{As}_2$. **b** Value of the elastoresistance coefficients \bar{m}_α at 40 K as a function of doping, for the three symmetry channels. The black triangles (right axis) represent the in-plane electronic Grüneisen parameter Γ , for comparison with $\bar{m}_{A_{1g}}$. Note the experimental definition^{34,48} $\Gamma_a \equiv \alpha_a^{\text{elec}}/C^{\text{elec}} = -(d\gamma/dp_a)/\gamma$ where p_a is the in-plane uniaxial pressure.

Methods

Sample Growth

Single crystals of CsFe_2As_2 were grown from solution using a Cs-rich self-flux in a sealed environment⁶⁵. Cs, Fe and As were weighted in molar ratio 8:1:11, respectively. All sample manipulations were performed in an argon glove box (O_2 content is < 0.5 ppm). Molten Cs together with a mixture of iron and arsenic powder were loaded into an alumina crucible. Typically 15–20 gr of a mixture of Cs, Fe and As were used for each crystal growth experiment. The alumina crucible with a lid was placed inside a stainless steel container and encapsulated. This was done by welding a stainless screw cap to one end of the container. This has the advantage that stainless steel does not corrode due to Cs vapour at high temperatures. The stainless steel container was placed in a tube furnace, which was evacuated at 5–10 mbar and slowly heated up to 200 °C. The sample was kept at this temperature for 10 h and subsequently heated up to 980 °C in 8 hours. The furnace temperature was kept constant at 980 °C for 5 h and slowly cooled to 760 °C in 14 days and then the furnace was canted to separate the excess flux. After cooling to room temperature, shiny plate-like crystals were easily removed from the remaining ingot. Refined crystallographic data have been presented elsewhere⁴⁵. KFe_2As_2 and RbFe_2As_2 single crystals were obtained under similar conditions using an alkali metal / As-rich flux³⁴.

High-quality single crystals of $\text{Ba}_{0.4}\text{K}_{0.6}\text{Fe}_2\text{As}_2$ were grown by a self-flux technique, using FeAs fluxes, in alumina crucibles sealed in iron cylinders using very slow cooling rates of 0.2–0.4 °C/hour. The crystals were annealed in-situ by further slow cooling to room temperature.

Elastoresistance measurements

Elastoresistance measurements were performed in a commercial strain cell (Razorbill Instruments CS-120). The samples were cut with edges along the tetragonal in-plane directions [100] or [110], with typical dimensions of $3.0 \times 1.0 \times 0.06$ mm. The

samples were fixed in the strain cell using DevCon 5 Minute Epoxy with an effective strained sample length of 2.0 mm. The epoxy thickness was controlled to be 50 μm below the sample and $\sim 30 \mu\text{m}$ above the sample. Cigarette paper was used to ensure electrical insulation of the sample from the titanium mounting plates. The sample strain was measured via a built-in capacitive displacement sensor and read out on an Andeen Hagerling 2550A capacitance bridge. Resistance was measured using a four-point method on a Lake Shore 372 resistance bridge. Hans Wolbring Leitsilber 200N was used to make the electrical contacts, as contacts made with DuPont 4929N silver paint were found to be mechanically unstable on strain application.

Due to the large thermal expansion mismatch between our samples and the titanium body of the strain cell, the samples will experience tension on cooling (Fig. 1b). In the most extreme case of CsFe_2As_2 , the sample is expected to experience $\sim 0.7\%$ tension at base temperature. In contrast, the parent compound BaFe_2As_2 has a thermal expansion nearly identical to titanium. This is also true for lightly-doped compounds⁶⁶. Elastoresistance has typically been measured by gluing the sample directly onto the side of a piezoelectric stack, which has a small thermal expansion, similar to titanium⁶⁷. The success of previous elastoresistance measurements on lightly doped BaFe_2As_2 samples thus depended on the fortunately similar thermal expansion of the piezoelectric stack and the sample. However, this method is unreliable for the $3d^{5.5}$ superconductors⁴⁵.

To keep the sample in an unstrained state on cooling, we progressively reduce the distance between the sample mounting plates by an amount calculated based on the known thermal expansion difference between the sample and titanium, and the measurement of a titanium calibration sample⁴⁵.

To express the elastoresistance in terms of the irreducible representations α of the D_{4h} point group, we note that the symmetric strains ϵ_α are given in terms of ϵ_{xx} by $\epsilon_{A_{1g}} = \frac{1}{2}(\epsilon_{[100]} + \epsilon_{[010]}) = \frac{1}{2}(\epsilon_{[110]} + \epsilon_{[\bar{1}\bar{1}0]})$, $\epsilon_{B_{1g}} = \frac{1}{2}(\epsilon_{[100]} - \epsilon_{[010]})$ and $\epsilon_{B_{2g}} = \frac{1}{2}(\epsilon_{[110]} - \epsilon_{[\bar{1}\bar{1}0]})$, where we use the simplified notation $\epsilon_x \equiv \epsilon_{xx}$. Similar expressions apply relating R_α with R_{xx} . The symmetry-decomposed elastoresistance coefficients are then defined as $m_\alpha = (1/R_\alpha)dR_\alpha/d\epsilon_\alpha$. In terms of the experimental data, these coefficients are given by

$$\begin{aligned} m_{A_{1g}} &= \frac{1}{1 - \nu_{[100]}} \left[\frac{1}{R_{[100]}} \frac{dR_{[100]}}{d\epsilon_{[100]}} + \frac{1}{R_{[010]}} \frac{dR_{[010]}}{d\epsilon_{[100]}} \right] \\ &= \frac{1}{1 - \nu_{[110]}} \left[\frac{1}{R_{[110]}} \frac{dR_{[110]}}{d\epsilon_{[110]}} + \frac{1}{R_{[\bar{1}\bar{1}0]}} \frac{dR_{[\bar{1}\bar{1}0]}}{d\epsilon_{[110]}} \right] \\ m_{B_{1g}} &= \frac{1}{1 + \nu_{[100]}} \left[\frac{1}{R_{[100]}} \frac{dR_{[100]}}{d\epsilon_{[100]}} - \frac{1}{R_{[010]}} \frac{dR_{[010]}}{d\epsilon_{[100]}} \right] \\ m_{B_{2g}} &= \frac{1}{1 + \nu_{[110]}} \left[\frac{1}{R_{[110]}} \frac{dR_{[110]}}{d\epsilon_{[110]}} - \frac{1}{R_{[\bar{1}\bar{1}0]}} \frac{dR_{[\bar{1}\bar{1}0]}}{d\epsilon_{[110]}} \right]. \end{aligned}$$

The quantity ν is the sample's Poisson ratio, which relates the strain along different directions, $\nu_{[100]} = -\epsilon_{[010]}/\epsilon_{[100]}$, and $\nu_{[110]} = -\epsilon_{[\bar{1}\bar{1}0]}/\epsilon_{[110]}$. In general, ν is sample and temperature dependent and anisotropic ($\nu_{[100]} \neq \nu_{[110]}$). The elastoresistance coefficients in the notation of irreducible representations are given in terms of the elastoresistance coefficients in the usual Voigt notation as

$$\begin{aligned} m_{B_{1g}} &= m_{11} - m_{12} \\ m_{B_{2g}} &= 2m_{66} \\ m_{A_{1g}} &= (m_{11} + m_{12}) - \frac{2\nu'}{1 - \nu} m_{13} \\ &= m_{A_{1g,1}} - \frac{2\nu'}{1 - \nu} m_{A_{1g,2}} \end{aligned}$$

In the A_{1g} channel, $m_{13} = m_{A_{1g,2}}$ contributes and cannot be disentangled from $m_{11} + m_{12} = m_{A_{1g,1}}$. Our measured elastoresistance coefficient $m_{A_{1g}}$ therefore includes the effect of c -axis compression (tension) which accompanies the symmetric in-plane biaxial tension (compression) because of the Poisson effect.

	c_{11}	c_{12}	c_{13}	c_{33}	c_{66}	$v_{[100]}$	$v'_{[100]}$	$v_{[110]}$	$v'_{[110]}$
Ba _{0.5} K _{0.5} Fe ₂ As ₂	123.1	51.3	66.2	92.2	51.0	0.049	0.682	-0.126	0.808
KFe ₂ As ₂	79.7	46.6	38.4	45.1	31.5	0.296	0.600	-0.017	0.866
RbFe ₂ As ₂	78.3	40.2	28.4	53.8	33.2	0.398	0.318	0.143	0.453
CsFe ₂ As ₂	84.4	45.9	39.5	61.2	31.6	0.346	0.422	0.113	0.572

Table 1. Table of elastic constants (in units of GPa) and Poisson ratios (unitless), obtained from ab-initio calculations.

Calculation of Poisson ratios

The sample Poisson ratios $v_x = -\epsilon_{yy}/\epsilon_{xx}$ and $v'_x = -\epsilon_{zz}/\epsilon_{xx}$ in terms of the elastic constants c_{ij} are given by

$$v_{[100]} = \frac{c_{13}^2 - c_{12}c_{33}}{c_{13}^2 - c_{11}c_{33}}$$

$$v'_{[100]} = \frac{(c_{12} - c_{11})c_{13}}{c_{13}^2 - c_{11}c_{33}}$$

$$v_{[110]} = \frac{c_{33}(c_{11} + c_{12} - 2c_{66}) - 2c_{13}^2}{c_{33}(c_{11} + c_{12} + 2c_{66}) - 2c_{13}^2}$$

$$v'_{[110]} = \frac{4c_{13}c_{66}}{c_{33}(c_{11} + c_{12} + 2c_{66}) - 2c_{13}^2}.$$

To obtain rough estimates of the elastic constants, we performed ab-initio calculations in the framework of the generalized gradient approximation using a mixed-basis pseudopotential method³⁶. The phonon dispersions and corresponding inter-atomic force constants were calculated via density functional perturbation theory and the elastic constants were then extracted via the method of long waves. For Ba_{0.4}K_{0.6}Fe₂As₂, we used values calculated for Ba_{0.5}K_{0.5}Fe₂As₂ in a virtual-crystal approximation. The numerical values of elastic constants and Poisson ratios calculated therefrom are given in Table 1. For the purposes of calculating the elastoresistance coefficients, the Poisson ratios were taken to be temperature independent.

References

1. Kuo, H.-H., Chu, J.-H., Palmstrom, J. C., Kivelson, S. A. & Fisher, I. R. Ubiquitous signatures of nematic quantum criticality in optimally doped Fe-based superconductors. *Science* **352**, 958–962, DOI: [10.1126/science.aab0103](https://science.sciencemag.org/content/352/6288/958.full.pdf) (2016). <https://science.sciencemag.org/content/352/6288/958.full.pdf>.
2. Fernandes, R. M., Chubukov, A. V. & Schmalian, J. What drives nematic order in iron-based superconductors? *Nat. Phys.* **10**, 97–104, DOI: [10.1038/nphys2877](https://doi.org/10.1038/nphys2877) (2014).
3. Kivelson, S. A., Fradkin, E. & Emery, V. J. Electronic liquid-crystal phases of a doped Mott insulator. *Nature* **393**, 550–553, DOI: [10.1038/31177](https://doi.org/10.1038/31177) (1998).
4. Hinkov, V. *et al.* Electronic liquid crystal state in the high-temperature superconductor YBa₂Cu₃O_{6.45}. *Science* **319**, 597–600, DOI: [10.1126/science.1152309](https://doi.org/10.1126/science.1152309) (2008).
5. Daou, R. *et al.* Broken rotational symmetry in the pseudogap phase of a high- T_c superconductor. *Nature* **463**, 519–522, DOI: [10.1038/nature08716](https://doi.org/10.1038/nature08716) (2010).
6. Murayama, H. *et al.* Diagonal nematicity in the pseudogap phase of HgBa₂CuO_{4+δ}. *Nat. Commun.* **10**, DOI: [10.1038/s41467-019-11200-1](https://doi.org/10.1038/s41467-019-11200-1) (2019).
7. Sato, Y. *et al.* Thermodynamic evidence for a nematic phase transition at the onset of the pseudogap in YBa₂Cu₃O_y. *Nat. Phys.* **13**, 1074–1078, DOI: [10.1038/nphys4205](https://doi.org/10.1038/nphys4205) (2017).
8. Achkar, A. J. *et al.* Nematicity in stripe-ordered cuprates probed via resonant x-ray scattering. *Science* **351**, 576–578, DOI: [10.1126/science.aad1824](https://doi.org/10.1126/science.aad1824) (2016).
9. Cyr-Choinière, O. *et al.* Two types of nematicity in the phase diagram of the cuprate superconductor YBa₂Cu₃O_y. *Phys. Rev. B* **92**, 224502, DOI: [10.1103/PhysRevB.92.224502](https://doi.org/10.1103/PhysRevB.92.224502) (2015).
10. Lawler, M. J. *et al.* Intra-unit-cell electronic nematicity of the high- T_c copper-oxide pseudogap states. *Nature* **466**, 347–351, DOI: [10.1038/nature09169](https://doi.org/10.1038/nature09169) (2010).

11. Vojta, M. Lattice symmetry breaking in cuprate superconductors: stripes, nematics, and superconductivity. *Adv. Phys.* **58**, 699–820, DOI: [10.1080/00018730903122242](https://doi.org/10.1080/00018730903122242) (2009).
12. Auvray, N. *et al.* Nematic fluctuations in the cuprate superconductor $\text{Bi}_2\text{Sr}_2\text{CaCu}_2\text{O}_{8+\delta}$. *Nat. Commun.* **10**, DOI: [10.1038/s41467-019-12940-w](https://doi.org/10.1038/s41467-019-12940-w) (2019).
13. Ronning, F. *et al.* Electronic in-plane symmetry breaking at field-tuned quantum criticality in CeRhIn_5 . *Nature* **548**, 313–317, DOI: [10.1038/nature23315](https://doi.org/10.1038/nature23315) (2017).
14. Helm, T. *et al.* Non-monotonic pressure dependence of high-field nematicity and magnetism in CeRhIn_5 . *Nat. Commun.* **11**, DOI: [10.1038/s41467-020-17274-6](https://doi.org/10.1038/s41467-020-17274-6) (2020).
15. Yonezawa, S. *et al.* Thermodynamic evidence for nematic superconductivity in $\text{Cu}_x\text{Bi}_2\text{Se}_3$. *Nat. Phys.* **13**, 123–126, DOI: [10.1038/nphys3907](https://doi.org/10.1038/nphys3907) (2016).
16. Shen, J. *et al.* Nematic topological superconducting phase in Nb-doped Bi_2Se_3 . *npj Quantum Mater.* **2**, DOI: [10.1038/s41535-017-0064-1](https://doi.org/10.1038/s41535-017-0064-1) (2017).
17. Hecker, M. & Schmalian, J. Vestigial nematic order and superconductivity in the doped topological insulator $\text{Cu}_x\text{Bi}_2\text{Se}_3$. *npj Quantum Mater.* **3**, DOI: [10.1038/s41535-018-0098-z](https://doi.org/10.1038/s41535-018-0098-z) (2018).
18. woo Cho, C. *et al.* Z_3 -vestigial nematic order due to superconducting fluctuations in the doped topological insulators $\text{Nb}_x\text{Bi}_2\text{Se}_3$ and $\text{Cu}_x\text{Bi}_2\text{Se}_3$. *Nat. Commun.* **11**, DOI: [10.1038/s41467-020-16871-9](https://doi.org/10.1038/s41467-020-16871-9) (2020).
19. Cao, Y. *et al.* Nematicity and competing orders in superconducting magic-angle graphene (2020). [2004.04148](https://arxiv.org/abs/2004.04148).
20. Eckberg, C. *et al.* Sixfold enhancement of superconductivity in a tunable electronic nematic system. *Nat. Phys.* **16**, 346–350, DOI: [10.1038/s41567-019-0736-9](https://doi.org/10.1038/s41567-019-0736-9) (2019).
21. Malinowski, P. *et al.* Suppression of superconductivity by anisotropic strain near a nematic quantum critical point. *Nat. Phys.* **16**, 1189–1193, DOI: [10.1038/s41567-020-0983-9](https://doi.org/10.1038/s41567-020-0983-9) (2020).
22. Lederer, S., Schattner, Y., Berg, E. & Kivelson, S. A. Enhancement of superconductivity near a nematic quantum critical point. *Phys. Rev. Lett.* **114**, 097001, DOI: [10.1103/PhysRevLett.114.097001](https://doi.org/10.1103/PhysRevLett.114.097001) (2015).
23. Lederer, S., Schattner, Y., Berg, E. & Kivelson, S. A. Superconductivity and non-Fermi liquid behavior near a nematic quantum critical point. *Proc. Natl. Acad. Sci.* **114**, 4905–4910, DOI: [10.1073/pnas.1620651114](https://doi.org/10.1073/pnas.1620651114) (2017).
24. Nandi, S. *et al.* Anomalous suppression of the orthorhombic lattice distortion in superconducting $\text{Ba}(\text{Fe}_{1-x}\text{Co}_x)_2\text{As}_2$ single crystals. *Phys. Rev. Lett.* **104**, 057006, DOI: [10.1103/PhysRevLett.104.057006](https://doi.org/10.1103/PhysRevLett.104.057006) (2010).
25. Chu, J.-H., Kuo, H.-H., Analytis, J. G. & Fisher, I. R. Divergent nematic susceptibility in an iron arsenide superconductor. *Science* **337**, 710–712, DOI: [10.1126/science.1221713](https://doi.org/10.1126/science.1221713) (2012).
26. Gallais, Y. *et al.* Observation of incipient charge nematicity in $\text{Ba}(\text{Fe}_{1-x}\text{Co}_x)_2\text{As}_2$. *Phys. Rev. Lett.* **111**, 267001, DOI: [10.1103/PhysRevLett.111.267001](https://doi.org/10.1103/PhysRevLett.111.267001) (2013).
27. Böhmer, A. *et al.* Nematic susceptibility of hole-doped and electron-doped BaFe_2As_2 iron-based superconductors from shear modulus measurements. *Phys. Rev. Lett.* **112**, 047001, DOI: [10.1103/PhysRevLett.112.047001](https://doi.org/10.1103/PhysRevLett.112.047001) (2014).
28. Chu, J.-H., Kuo, H.-H., Analytis, J. G. & Fisher, I. R. Divergent nematic susceptibility in an iron arsenide superconductor. *Science* **337**, 710–712, DOI: [10.1126/science.1221713](https://doi.org/10.1126/science.1221713) (2012). <https://science.sciencemag.org/content/337/6095/710.full.pdf>.
29. Ikeda, M. S. *et al.* Elastocaloric signature of nematic fluctuations (2020). [2101.00080](https://arxiv.org/abs/2101.00080).
30. de' Medici, L., Hassan, S. R., Capone, M. & Dai, X. Orbital-selective Mott transition out of band degeneracy lifting. *Phys. Rev. Lett.* **102**, 126401, DOI: [10.1103/PhysRevLett.102.126401](https://doi.org/10.1103/PhysRevLett.102.126401) (2009).
31. Misawa, T., Nakamura, K. & Imada, M. Ab initio evidence for strong correlation associated with Mott proximity in iron-based superconductors. *Phys. Rev. Lett.* **108**, 177007, DOI: [10.1103/PhysRevLett.108.177007](https://doi.org/10.1103/PhysRevLett.108.177007) (2012).
32. de' Medici, L., Giovannetti, G. & Capone, M. Selective Mott physics as a key to iron superconductors. *Phys. Rev. Lett.* **112**, 177001, DOI: [10.1103/PhysRevLett.112.177001](https://doi.org/10.1103/PhysRevLett.112.177001) (2014).
33. Hardy, F. *et al.* Evidence of strong correlations and coherence-incoherence crossover in the iron pnictide superconductor KFe_2As_2 . *Phys. Rev. Lett.* **111**, 027002, DOI: [10.1103/PhysRevLett.111.027002](https://doi.org/10.1103/PhysRevLett.111.027002) (2013).
34. Hardy, F. *et al.* Strong correlations, strong coupling, and s-wave superconductivity in hole-doped BaFe_2As_2 single crystals. *Phys. Rev. B* **94**, 205113, DOI: [10.1103/PhysRevB.94.205113](https://doi.org/10.1103/PhysRevB.94.205113) (2016).

35. Wu, Y. *et al.* Emergent Kondo lattice behavior in iron-based superconductors AFe_2As_2 ($A = \text{K, Rb, Cs}$). *Phys. Rev. Lett.* **116**, 147001, DOI: [10.1103/PhysRevLett.116.147001](https://doi.org/10.1103/PhysRevLett.116.147001) (2016).
36. Eilers, F. *et al.* Strain-driven approach to quantum criticality in AFe_2As_2 with $A = \text{K, Rb, and Cs}$. *Phys. Rev. Lett.* **116**, 237003, DOI: [10.1103/PhysRevLett.116.237003](https://doi.org/10.1103/PhysRevLett.116.237003) (2016).
37. Zhang, Z. T. *et al.* Increasing stripe-type fluctuations in AFe_2As_2 ($A = \text{K, Rb, Cs}$) superconductors probed by ^{75}As NMR spectroscopy. *Phys. Rev. B* **97**, 115110, DOI: [10.1103/PhysRevB.97.115110](https://doi.org/10.1103/PhysRevB.97.115110) (2018).
38. Li, J. *et al.* Reemergeing electronic nematicity in heavily hole-doped Fe-based superconductors (2016). [1611.04694](https://arxiv.org/abs/1611.04694).
39. Ishida, K. *et al.* Novel electronic nematicity in heavily hole-doped iron pnictide superconductors. *Proc. Natl. Acad. Sci.* **117**, 6424–6429, DOI: [10.1073/pnas.1909172117](https://doi.org/10.1073/pnas.1909172117) (2020). <https://www.pnas.org/content/117/12/6424.full.pdf>.
40. Liu, X. *et al.* Evidence of nematic order and nodal superconducting gap along $[110]$ direction in RbFe_2As_2 . *Nat. Commun.* **10**, DOI: [10.1038/s41467-019-08962-z](https://doi.org/10.1038/s41467-019-08962-z) (2019).
41. Onari, S. & Kontani, H. Origin of diverse nematic orders in fe-based superconductors: 45° rotated nematicity in AFe_2As_2 ($A = \text{Cs, Rb}$). *Phys. Rev. B* **100**, 020507, DOI: [10.1103/PhysRevB.100.020507](https://doi.org/10.1103/PhysRevB.100.020507) (2019).
42. Wang, Y., Hu, W., Yu, R. & Si, Q. Broken mirror symmetry, incommensurate spin correlations, and B_{2g} nematic order in iron pnictides. *Phys. Rev. B* **100**, 100502, DOI: [10.1103/PhysRevB.100.100502](https://doi.org/10.1103/PhysRevB.100.100502) (2019).
43. Borisov, V., Fernandes, R. M. & Valentí, R. Evolution from B_{2g} nematics to B_{1g} nematics in heavily hole-doped iron-based superconductors. *Phys. Rev. Lett.* **123**, 146402, DOI: [10.1103/PhysRevLett.123.146402](https://doi.org/10.1103/PhysRevLett.123.146402) (2019).
44. Moroni, M. *et al.* Charge and nematic orders in AFe_2As_2 ($A = \text{Rb, Cs}$) superconductors. *Phys. Rev. B* **99**, 235147, DOI: [10.1103/PhysRevB.99.235147](https://doi.org/10.1103/PhysRevB.99.235147) (2019).
45. Wiecki, P. *et al.* Dominant in-plane symmetric elastoresistance in CsFe_2As_2 . *Phys. Rev. Lett.* **125**, 187001, DOI: [10.1103/PhysRevLett.125.187001](https://doi.org/10.1103/PhysRevLett.125.187001) (2020).
46. Kuo, H.-H., Shapiro, M. C., Riggs, S. C. & Fisher, I. R. Measurement of the elastoresistivity coefficients of the underdoped iron arsenide $\text{Ba}(\text{Fe}_{0.975}\text{Co}_{0.025})_2\text{As}_2$. *Phys. Rev. B* **88**, 085113, DOI: [10.1103/PhysRevB.88.085113](https://doi.org/10.1103/PhysRevB.88.085113) (2013).
47. Palmstrom, J. C., Hristov, A. T., Kivelson, S. A., Chu, J.-H. & Fisher, I. R. Critical divergence of the symmetric (A_{1g}) nonlinear elastoresistance near the nematic transition in an iron-based superconductor. *Phys. Rev. B* **96**, 205133, DOI: [10.1103/PhysRevB.96.205133](https://doi.org/10.1103/PhysRevB.96.205133) (2017).
48. Meingast, C. *et al.* Thermal expansion and Grüneisen parameters of $\text{Ba}(\text{Fe}_{1-x}\text{Co}_x)_2\text{As}_2$: A thermodynamic quest for quantum criticality. *Phys. Rev. Lett.* **108**, 177004, DOI: [10.1103/PhysRevLett.108.177004](https://doi.org/10.1103/PhysRevLett.108.177004) (2012).
49. Backes, S., Jeschke, H. O. & Valentí, R. Microscopic nature of correlations in multiorbital AFe_2As_2 ($A = \text{K, Rb, Cs}$): Hund's coupling versus coulomb repulsion. *Phys. Rev. B* **92**, 195128, DOI: [10.1103/PhysRevB.92.195128](https://doi.org/10.1103/PhysRevB.92.195128) (2015).
50. Taufour, V. *et al.* Upper critical field of KFe_2As_2 under pressure: A test for the change in the superconducting gap structure. *Phys. Rev. B* **89**, 220509, DOI: [10.1103/PhysRevB.89.220509](https://doi.org/10.1103/PhysRevB.89.220509) (2014).
51. Rosenberg, E. W., Chu, J.-H., Ruff, J. P. C., Hristov, A. T. & Fisher, I. R. Divergence of the quadrupole-strain susceptibility of the electronic nematic system YbRu_2Ge_2 . *Proc. Natl. Acad. Sci.* **116**, 7232–7237, DOI: [10.1073/pnas.1818910116](https://doi.org/10.1073/pnas.1818910116) (2019). <https://www.pnas.org/content/116/15/7232.full.pdf>.
52. Küchler, R. *et al.* Grüneisen ratio divergence at the quantum critical point in $\text{CeCu}_{6-x}\text{Ag}_x$. *Phys. Rev. Lett.* **93**, 096402, DOI: [10.1103/PhysRevLett.93.096402](https://doi.org/10.1103/PhysRevLett.93.096402) (2004).
53. Garst, M. & Rosch, A. Sign change of the Grüneisen parameter and magnetocaloric effect near quantum critical points. *Phys. Rev. B* **72**, 205129, DOI: [10.1103/PhysRevB.72.205129](https://doi.org/10.1103/PhysRevB.72.205129) (2005).
54. Blomberg, E. C. *et al.* Sign-reversal of the in-plane resistivity anisotropy in hole-doped iron pnictides. *Nat. Commun.* **4**, DOI: [10.1038/ncomms2933](https://doi.org/10.1038/ncomms2933) (2013).
55. Böhmer, A. E. *et al.* Evolution of nematic fluctuations in $\text{CaK}(\text{Fe}_{1-x}\text{Ni}_x)_4\text{As}_4$ with spin-vortex crystal magnetic order (2020). [2011.13207](https://arxiv.org/abs/2011.13207).
56. Terashima, T. *et al.* Elastoresistance measurements on $\text{CaKFe}_4\text{As}_4$ and $\text{KCa}_2\text{Fe}_4\text{As}_4\text{F}_2$ with the Fe site of C_{2v} symmetry. *Phys. Rev. B* **102**, 054511, DOI: [10.1103/PhysRevB.102.054511](https://doi.org/10.1103/PhysRevB.102.054511) (2020).
57. Xu, N. *et al.* Possible nodal superconducting gap and Lifshitz transition in heavily hole-doped $\text{Ba}_{0.1}\text{K}_{0.9}\text{Fe}_2\text{As}_2$. *Phys. Rev. B* **88**, 220508, DOI: [10.1103/PhysRevB.88.220508](https://doi.org/10.1103/PhysRevB.88.220508) (2013).

58. Malaeb, W. *et al.* Abrupt change in the energy gap of superconducting $\text{Ba}_{1-x}\text{K}_x\text{Fe}_2\text{As}_2$ single crystals with hole doping. *Phys. Rev. B* **86**, 165117, DOI: [10.1103/PhysRevB.86.165117](https://doi.org/10.1103/PhysRevB.86.165117) (2012).
59. Liu, Y. & Lograsso, T. A. Crossover in the magnetic response of single-crystalline $\text{Ba}_{1-x}\text{K}_x\text{Fe}_2\text{As}_2$ and Lifshitz critical point evidenced by Hall effect measurements. *Phys. Rev. B* **90**, 224508, DOI: [10.1103/PhysRevB.90.224508](https://doi.org/10.1103/PhysRevB.90.224508) (2014).
60. Hodovanets, H. *et al.* Fermi surface reconstruction in $(\text{Ba}_{1-x}\text{K}_x)\text{Fe}_2\text{As}_2$ ($0.44 \leq x \leq 1$) probed by thermoelectric power measurements. *Phys. Rev. B* **89**, 224517, DOI: [10.1103/PhysRevB.89.224517](https://doi.org/10.1103/PhysRevB.89.224517) (2014).
61. Maiti, S. & Chubukov, A. V. $s + is$ state with broken time-reversal symmetry in Fe-based superconductors. *Phys. Rev. B* **87**, 144511, DOI: [10.1103/PhysRevB.87.144511](https://doi.org/10.1103/PhysRevB.87.144511) (2013).
62. Böker, J., Volkov, P. A., Efetov, K. B. & Eremin, I. $s + is$ superconductivity with incipient bands: Doping dependence and STM signatures. *Phys. Rev. B* **96**, 014517, DOI: [10.1103/PhysRevB.96.014517](https://doi.org/10.1103/PhysRevB.96.014517) (2017).
63. Grinenko, V. *et al.* Superconductivity with broken time-reversal symmetry inside a superconducting s -wave state. *Nat. Phys.* **16**, 789–794, DOI: [10.1038/s41567-020-0886-9](https://doi.org/10.1038/s41567-020-0886-9) (2020).
64. Wang, L. *et al.* Electronic nematicity in Uru_2Si_2 revisited. *Phys. Rev. Lett.* **124**, 257601, DOI: [10.1103/PhysRevLett.124.257601](https://doi.org/10.1103/PhysRevLett.124.257601) (2020).
65. Wang, A. F. *et al.* Calorimetric study of single-crystal CsFe_2As_2 . *Phys. Rev. B* **87**, 214509, DOI: [10.1103/PhysRevB.87.214509](https://doi.org/10.1103/PhysRevB.87.214509) (2013).
66. Ikeda, M. S. *et al.* Symmetric and antisymmetric strain as continuous tuning parameters for electronic nematic order. *Phys. Rev. B* **98**, 245133, DOI: [10.1103/PhysRevB.98.245133](https://doi.org/10.1103/PhysRevB.98.245133) (2018).
67. Böhmer, A. E. & Meingast, C. (unpublished).

Acknowledgements

We thank I. R. Fisher and K. Grube for valuable discussions. We acknowledge support by the Helmholtz Association under Contract No. VH-NG-1242.

Author contributions

P.W. and A.E.B. initiated the project. A.A.H. and T.W. grew single crystal samples. P.W., A.E.B. and M.F. performed the experiments. R.H. performed DFT calculations of elastic constants. P.W. analysed the data and P.W., C.M. and A.E.B. developed the interpretations. A.E.B. guided the project. P.W. and A.E.B. wrote the manuscript with input from all authors.